Partitioning of U and Th during garnet pyroxenite partial melting: Constraints on the source of alkaline ocean island basalts

L.J. Elkins *, G.A. Gaetani, K.W.W. Sims

Woods Hole Oceanographic Institution, Woods Hole, MA 02543, United States

Abstract

Uranium series disequilibria in ocean island basalts (OIB) provide evidence for the presence of garnet in their source region. It has been suggested that enriched OIB signatures derive from mantle lithologies other than peridotite, such as eclogite or pyroxenite, and, in particular, that silica-poor garnet pyroxenite is the source lithology for alkali basalts. To test the ability of such a source to produce the U–Th disequilibria observed in alkali OIB, we determined experimentally clinopyroxene-melt and garnet-melt partition coefficients for a suite of trace elements, including U and Th, at 2.5 GPa and 1420–1450 °C. The starting composition for the experiments was a 21% partial melt of a silica-poor garnet pyroxenite. Experimentally determined clinopyroxene-melt partition coefficients range from 0.0083 ± 0.0006 to 0.020 ± 0.002 for Th and from 0.0094 ± 0.0006 to 0.024 ± 0.002 for U, and garnet-melt partition coefficients are 0.0032 ± 0.0004 for Th and 0.013 ± 0.002 for U. Comparison of our experimental results with partition coefficients from previous experimental studies shows that the relative compatibilities of U and Th in both garnet and clinopyroxene are different for different mineral compositions, leading to varying degrees of U/Th fractionation with changing lithology. For a given melting rate and extent of partial melting, mafic lithologies tend to produce larger ^{230}Th excesses than peridotite. However, this effect is minimized by the greater overall extents of melting experienced by eclogites and pyroxenites relative to peridotite. Results from chromatographic, batch, and fractional melting calculations with binary mixing between partial melts of pyroxenite and peridotite, carried out using our new partitioning data for the pyroxenite component and taking into account variable productivities and different solidus depths for the two lithologies, suggest that OIB are not the product of progressive melting of a source containing a fixed quantity of garnet pyroxenite. Melting a peridotite with enriched signatures, and mixing those melts with melts of a depleted, "normal" peridotite, is an alternative explanation for the trends seen in Hawaiian, Azores and Samoan lavas.
© 2007 Elsevier B.V. All rights reserved.

Keywords: melting; uranium series; partition coefficients; garnet; clinopyroxene; garnet pyroxenite

1. Introduction

Most mid-ocean ridge basalts (MORB) and ocean island basalts (OIB) are not in secular equilibrium with respect to the uranium decay series isotopes. Observed (^{230}Th) excesses relative to (^{238}U) (where parentheses

---

 * Corresponding author. Tel.: +1 508 289 3422; fax: +1 508 457 2187.

   E-mail addresses: lelkins@whoi.edu (L.J. Elkins), ggaetani@whoi.edu (G.A. Gaetani), ksims@whoi.edu (K.W.W. Sims).

denote activity) indicate that Th generally behaves less compatibly during partial melting than U (e.g. (Bourdon et al., 1996). Garnet (Gt) and clinopyroxene (Cpx) are the principal hosts for U and Th in upper mantle rocks and, therefore, control the behavior of those elements during partial melting. Experimental determinations of mineral-melt partition coefficients ($D_i^{Mineral/Melt} = c_i^{Mineral}/c_i^{Melt}$, where c_i is the weight concentration of element i in the mineral or the melt) indicate that U is more compatible than Th in Gt during partial melting (i.e. $D_{Th}^{Gt/Melt}/D_U^{Gt/Melt} < 1$), whereas $D_{Th}^{Cpx/Melt}/D_U^{Cpx/Melt}$ is typically greater than 1 (e.g. (La Tourette and Burnett, 1992; Beattie, 1993a,b; La Tourette et al., 1993; Hauri et al., 1994). Thus, the presence of ^{230}Th excesses in MORB and OIB is generally taken as an indication of residual Gt in their source regions (e.g. (Bourdon et al., 1996). Whether that Gt resides in peridotite, pyroxenite, eclogite, or some combination thereof remains a matter of debate (e.g. Hirschmann and Stolper, 1996; Lundstrom et al., 1999; Stracke et al., 1999).

The long-lived radiogenic isotopic compositions of OIB indicate that the upper mantle is characterized by trace element heterogeneity (Zindler and Hart, 1986), suggesting that lithologic heterogeneity is also plausible. Because the relative compatibilities of U and Th during partial melting are sensitive to the major element compositions of the solid phases, a detailed understanding of mineral-melt partitioning of U and Th for a range of mafic and ultramafic lithologies (i.e. eclogite, pyroxenite, and peridotite) is necessary to evaluate the importance of each of those rock types in the melt generation process.

The major element compositions of melts produced by partial fusion of eclogites and pyroxenites at upper mantle conditions have been investigated experimentally in a number of studies, and it has been demonstrated that partial melting of silica-poor garnet pyroxenites can produce alkaline basaltic melts (Hirschmann et al., 2003; Pertermann and Hirschmann, 2003; Kogiso et al., 2004). This supports the suggestion that the melting of less abundant mantle lithologies such as eclogite and pyroxenite may play an important role in generating OIB (Hauri, 1996; Sigmarsson et al., 1998; Lassiter et al., 2000; Kogiso and Hirschmann, 2001; Hauri, 2002; Hirschmann et al., 2003; Kogiso et al., 2003, 2004). Clinopyroxenes and Gt in pyroxenites, eclogites, and peridotites have distinct compositions, however, raising the possibility that there may be systematic differences in the fractionation of U from Th during partial melting of these three lithologies. Partition coefficients for Cpx and Gt appropriate for peridotite partial melting have been experimentally determined over a wide range of temperature and pressure con-

ditions (Salters and Longhi, 1999; Salters et al., 2002). Pertermann and Hirschmann (2002) and Pertermann et al. (2004) also measured $D_i^{Mineral/Melt}$ values appropriate for partial melting of MORB-type eclogites that produce silica-rich melts. However, none of the existing experimental studies have generated the partitioning data needed to test whether silica-poor garnet pyroxenite is a realistic source for alkaline basaltic lavas, as suggested by Kogiso et al. (2004).

In this study, partition coefficients for Cpx and Gt compositions appropriate for partial melting of silica-poor garnet pyroxenite were determined experimentally at 2.5 GPa. We focus on the partitioning behavior of U and Th and use our experimental results to test the capacity of garnet pyroxenite to generate the (^{230}Th/^{238}U) disequilibria observed in alkaline OIB. We find that the relative compatibilities of U and Th in both Gt and Cpx and, thus, U/Th fractionation during partial melting, are different for different source lithologies. For a given melting rate and extent of partial melting, mafic lithologies tend to produce larger ^{230}Th excesses than peridotite. However, this effect is damped by the greater overall extents of melting experienced by eclogites and pyroxenites relative to peridotite. Mixtures of partial melts from peridotite and silica-poor garnet pyroxenite are capable of producing the range of ^{230}Th excesses and, for the most part, Sm and Nd fractionations and ε_{Nd} values found in OIB lavas. However, a peridotite source with an enriched trace element and isotopic composition could possibly explain the data as well. As noted by Stracke et al. (1999), trends formed by ocean island lavas from Hawaii in diagrams using these variables have the opposite sense of that expected from progressive melting with pyroxenite in the source. This additional constraint argues against pyroxenite in the source of Hawaii.

2. Experimental and analytical techniques

2.1. Starting materials

To examine the partitioning behavior of incompatible trace elements during partial fusion of silica-poor garnet pyroxenite, we experimentally determined $D_i^{Cpx/Melt}$ and $D_i^{Gt/Melt}$ values for 21% partial melting of pyroxenite MIX-1G at 2.5 GPa, previously studied by Hirschmann et al. (2003) and Kogiso et al. (2003). This bulk composition was found by Kogiso et al. (2003) to produce alkaline basalts during partial melting at upper mantle conditions. The melt composition from experiment 95MMH15 reported by Hirschmann et al. (2003) (see Table 1 in the Appendix) was synthesized as the starting mix PX21 from a combination of high-purity

Table 1
Experimental conditions, phase assemblages and phase proportions

Experiment	P (GPa)	T (°C)	Duration (h)	Run products	Phase proportions [b] (wt.%)
PX21f-4	2.5	1440	120	Gl, Cpx, Gt	76.5% Gl; 14.1% Cpx; 8.8% Gt; 0.17
PX21f-5	2.5	1450	144	Gl, Cpx	91.4% Gl; 7.8% Cpx; 1.24
PX21f-17	2.5	1440 [a]	72	Gl, Cpx, Sp	91.7% Gl; 6.8% Cpx; 0.2%Sp; 3.19
PX21g-2	2.5	1420	48	Gl, Cpx, Sp	90.4% Gl; 7.4% Cpx; 1.0% Sp; 1.07
PX21h-2	2.5	1420	48	Gl, Cpx, Sp	86.7% Gl; 11.2% Cpx; 1.2% Sp; 0.76

[a] Held at 1340 °C for 6 h before ramping up to 1440 °C.
[b] Calculated phase proportions for major element phase analyses (Table 3). Final value shown is mean sum of squares for mass balance analysis.

oxides and carbonates and homogenized by grinding in an agate mortar and pestle under ethanol for 6 h. The mix was then decarbonated at 850 °C, re-ground under ethanol, glassed for 10 min at 1200 °C in air in a vertical gas-mixing furnace using a graphite crucible, and ground to a fine powder. The bulk composition of the starting material was determined by fusing an aliquot in a piston cylinder apparatus at 1400 °C and 1.0 GPa, then analyzing the resulting glass by electron microprobe using the protocol described below (composition of the mixture in Table 1 in the Appendix).

Trace elements were added to three different aliquots of the PX21 starting material to minimize potential isobaric interferences and maximize the ion probe trace element signal in the crystals. The combinations of trace elements used in this study are: (1) U and Th (mix f); (2) Li, Rb, Nd, U, Be, Sr, Sm, and Th (mix g); (3) B, Y, Hf, La, V, Zr, Ta, Lu, Cr, Nb, Ba, and Pb (mix h). Doping levels were ~1 wt.% total trace elements in each batch. Uranium and Th were added using nitric acid standard solutions, and all other elements were added as solid oxide or carbonate powders.

2.2. Experimental methods

We conducted experiments using a piston-cylinder apparatus with 1.27 cm-diameter assemblies (Boyd and England, 1960). For each experiment, starting materials were packed into a graphite capsule, which constrains the oxygen fugacity in the charge to be ~1.5 log units more reducing than the fayalite–magnetite–quartz (FMQ) oxygen buffer (Ulmer and Luth, 1991), thereby maintaining a reduced U valence state (U^{4+} versus U^{6+}). The capsule was placed inside an alumina sleeve and centered within a straight-walled graphite furnace using crushable MgO spacers. The pressure medium was sintered CaF_2. The friction correction for the assemblies was calibrated against the Ca-Tschermakite breakdown reaction at 1.2 to 1.4 GPa and 1300 °C (Hays, 1966) and determined to be less than the pressure uncertainty (±50 MPa), so that no

correction has been applied to the pressures reported in Table 1. Experiments were conducted using the cold piston-in technique (Johannes et al., 1971) and brought to the desired temperature at a rate of 1 °C/s. Temperatures were measured and controlled using $W_{97}Re_3$–$W_{75}Re_{25}$ thermocouples positioned above the sample capsule, with no correction for the effect of pressure on thermocouple EMF. The temperature difference between the position of the thermocouple bead and the center of the sample, determined using offset thermocouples, was 9 °C. We have corrected the temperatures reported in Table 1 for this difference. Temperatures measured by this method are thought to be accurate to within ±10 °C, and pressure is thought to be accurate to within ±0.5 GPa. Run durations ranged from 48 to 144 h, and experiments were quenched upon completion by shutting off the power.

2.3. Analytical methods

Experimental run products were longitudinally sectioned, mounted in epoxy, polished, and analyzed for major elements using the 5-spectrometer JEOL 733 electron microprobe at Massachusetts Institute of Technology. We used a 10 nA beam current and 15 kV accelerating potential for all analyses. Beam diameters of 10 μm and 1 μm were used for analyses of glass and crystalline phases, respectively. We measured elements in the glass using count times of 5 s for Na, 10 s for Mn and Fe and 40 s for Mg, Al, Si, Ti, K, and Ca. Peak counting times for pyroxene crystals were 15 s for Na and 40 s for Mn and Fe, and for Gt analyses were carried out by counting Na and Ti for 20 s and Mn and Fe for 40 s. Data were reduced using a modified ZAF procedure (Armstrong, 1988).

Trace element concentrations were measured by secondary ion mass spectrometry (SIMS) with the Cameca 3f ion microprobe at Woods Hole Oceanographic Institution. A ~0.1 nA primary O^- beam less than 5 μm in diameter was used for all analyses due to small Cpx grain sizes. A primary accelerating voltage of

8.2 keV with a secondary accelerating voltage of 4.41 keV produced a primary O^- beam impact energy of 12.61 keV. Following a 3–5 min. pre-burn to remove the Au coat, a single spot was occupied while measuring secondary ion intensities for [7]Li, [9]Be, [11]B, [51]V, [52]Cr, [85]Rb, [88]Sr, [89]Y, [90]Zr, [93]Nb, [138]Ba, [139]La, [146]Nd, [147]Sm, [175]Lu, [178]Hf, [181]Ta, [208]Pb, [232]Th, or [238]U within a 20 eV window centered on a 90 eV offset from the peak of the energy distribution. Count times of 20 s were used for all elements in experiments PX21g-2 and -h-2, except Hf, Ta, and Pb, which were measured for 30 s each. In experiments PX21f-4, -5, and -17, U and Th were measured with count times of 30 s. Trace element measurements were normalized to either [28]Si or [30]Si and calibrated against standards NIST-610 and NIST-612.

3. Experimental results

3.1. Partitioning experiments

Five experiments were carried out to determine partition coefficients for incompatible trace elements among Cpx, Gt, and nepheline-normative silicate melt during garnet pyroxenite partial melting at 2.5 GPa and 1420° to 1450 °C (Table 1). All experiments produced Cpx, spinel (Sp) and silicate melt. One of the experiments contains a mineral assemblage of Cpx+Gt+Sp, while the others contain Cpx+Sp only. The absence of Gt from all but one of the experiments, which were carried out using a single starting mix, is thought to be attributable to sluggish nucleation. All experiments contain large areas of homogeneous, quench growth-free glass.

The experiment conducted at 1450 °C (just below the liquidus temperature of 1455 °C inferred from experiment 95MMH15 of Hirschmann et al. (2003)) for 144 h contains 91 wt.% silicate melt, 9 wt.% Cpx (~20 μm), and a trace amount of Sp. An experiment held at 1440 °C for 120 h produced 77 wt.% silicate melt, 16 wt.% Cpx (~20–30 μm), 6 wt.% Gt (up to ~300 μm), many of which poikilitically enclose small pyroxene grains, and trace amounts of Sp. A second experiment conducted at 1440 °C was initially held at 1340 °C for 6 h, and then ramped up to 1440 °C at 1 °C/s to approach the same equilibrium from a different

Table 2
Electron microprobe analyses of experimental run products

Phase	n	SiO_2	TiO_2	Al_2O_3	Cr_2O_3	FeO	MnO	MgO	CaO	Na_2O	K_2O	P_2O_5	Total
Hirschmann et al. (2003)													
Gl	5	43.1(7)[a]	2.58(9)	14.20(2)	–	13.6(4)	0.15(3)	12.5(3)	10.2(1)	3.72(7)	0.08(2)	0.06(1)	100.2
Cpx	10	50.8(7)	0.51(2)	10.5(3)	–	5.4(1)	0.10(5)	16.7(1)	14.70(4)	1.2(1)	0.01(1)	0.00(1)	99.9
Gt	7	41.4(2)	0.52(6)	23.0(2)	–	8.2(1)	0.20(4)	19.1(1)	6.0(1)	0.02(2)	0.01(1)	0.02(3)	98.7
PX21f-4 — 1440 °C — 120 h													
Gl	9	41.9(2)	3.0(1)	13.8(1)	0.004(12)	15.0(2)	0.13(4)	11.2(2)	9.4(1)	4.7(3)	0.108(9)	0.03(3)	99.3
Cpx	20	49.5(3)	0.57(6)	11.6(2)	0.002(5)	6.6(3)	0.12(2)	15.6(3)	14.6(4)	1.96(6)	–	–	100.5
Gt	18	41.1(2)	0.55(3)	24.2(2)	0.03(2)	10.8(1)	0.22(4)	16.6(2)	5.7(1)	0.02(2)	–	–	99.1
PX21f-5 — 1450 °C — 144 h													
Gl	10	42.3(3)	2.7(2)	14.71(7)	0.01(2)	13.7(3)	0.17(5)	11.3(2)	9.48(6)	4.2(2)	0.1(1)	0.05(5)	98.8
Cpx	16	50.0(5)	0.48(4)	11.6(4)	0.02(1)	6.0(2)	0.11(2)	15.8(3)	14.8(5)	1.66(6)	–	–	100.5
PX21f-17 — 1440 °C — 72 h													
Gl	22	43.0(2)	2.7(1)	15.1(1)	0.01(2)	13.5(2)	0.17(5)	10.9(1)	9.75(6)	3.8(2)	0.11(1)	0.02(4)	99.2
Cpx	5	49.8(3)	0.53(6)	11.8(4)	0.02(2)	5.8(2)	0.12(2)	15.3(5)	15.5(3)	1.69(7)	–	–	100.6
Sp	8	1.2(1.1)	0.29(9)	65.5(1.4)	0.01(2)	12.5(3)	0.06(2)	20.1(3)	0.3(3)	–	–	–	100
PX21g-2 — 1420 °C — 48 h													
Gl	24	43.6(5)	2.7(1)	14.6(1)	0.04(4)	13.9(3)	0.19(4)	11.8(3)	9.30(7)	4.0(2)	0.11(1)	0.02(3)	100.2
Cpx	17	51.3(7)	0.43(8)	9.9(1.0)	0.00002(7)	6.5(4)	0.13(3)	17.9(1.1)	12.9(9)	1.6(1)	–	–	100.7
Sp	12	1.0(2.0)	0.26(3)	65.5(2.5)	0.002(4)	12.2(3)	0.09(2)	20.3(2)	0.2(5)	–	–	–	99.6
PX21h-2 — 1420 °C — 48 h													
Gl	18	43.4(2)	2.8(1)	14.7(1)	0.02(2)	14.3(3)	0.18(5)	11.5(3)	9.51(6)	4.2(2)	0.111(9)	0.006(12)	100.7
Cpx	9	50.7(6)	0.44(4)	10.2(9)	0	6.5(2)	0.12(2)	17.0(1.3)	13.6(1.0)	1.6(2)	–	–	100.3
Sp	15	0.32(2)	0.26(2)	64.8(4)	0	12.6(2)	0.06(3)	19.7(2)	0.008(5)	–	–	–	97.9

[a] Numbers in parentheses represent 1σ standard deviation in terms of least units cited on the basis of replicate analyses. Thus 43.1(7) should be read as 43.1±0.7

starting condition. This experiment produced 93 wt.% silicate melt, 7 wt.% Cpx (~ 20 µm), and a trace amount of Sp (~ 10 µm).

Additional experiments were conducted at 2.5 GPa and 1420 °C using starting compositions doped with a larger suite of trace elements (mixes g and h). The experiment doped with Li, Be, Rb, Sr, Nd, Sm, Th, and U contains 92 wt.% melt, 7 wt.% Cpx (~ 200–300 µm), and 1 wt.% Sp (~ 100–200 µm). Similarly, the experiment doped with B, V, Cr, Y, Zr, Nb, Ba, La, Lu, Hf, Ta, and Pb contains 87 wt.% silicate melt, 11 wt.% Cpx (~ 500 µm), and 1 wt.% Sp (~ 200 µm).

Major element compositions of silicate melts, Cpx, Gt, and Sp are reported in Table 2. Clinopyroxene, Gt, and melt compositions are similar to those reported from the pyroxenite partial melting experiments of Hirschmann et al. (2003). The silicate melts produced in our experiments are SiO_2-poor (41.9 ± 0.2 to 43.6 ± 0.5 wt.%) with 9.5 to 15.8 wt.% nepheline in their CIPW norms and molar $Mg/(Mg + \Sigma Fe)$ (Mg#) ranging from 0.57 to 0.60. Clinopyroxenes have moderately high Al_2O_3 and Na_2O contents (~ 11.0 wt.% and ~ 1.7 wt.%, respectively) resulting in a significant jadeite component. The principal difference between the Cpx in our experiments and those from Hirschmann et al. (2003) is that ours have lower Mg# (a mean of 0.822 ± 0.006 for the 5 experiments reported in Table 2, versus 0.846 ± 0.001 in Hirschmann

et al. (2003)), likely a result of the systematically lower temperatures at which our experiments were carried out.

Compared against experiments on U and Th partitioning during partial melting of eclogite, the Cpx from our experiments are characterized by lower TiO_2 (~ 0.50 versus ~ 3 wt.%), Al_2O_3 (~ 11 versus ~ 17 wt.%), and Na_2O (~ 2 versus ~ 4 wt.%), and higher Mg# (~ 0.82 versus ~ 0.66) (Pertermann and Hirschmann, 2002, 2003; Pertermann et al., 2004). The Cpx in our experiments have relatively higher Al_2O_3 (~ 11 versus ~ 8 wt.%), CaO (~ 14 versus ~ 10 wt.%), and Na_2O (~ 2 versus ~ 1 wt.%) and slightly lower Mg# (~ 0.82 versus ~ 0.88) than experiments looking at U and Th partitioning during peridotite partial melting (Salters and Longhi, 1999; Salters et al., 2002; McDade et al., 2003). Finally, compared with U and Th partitioning experiments conducted on near-liquidus basalts, the Cpx from our experiments have higher Al_2O_3 (~ 11 versus ~ 7 wt.%) and Na_2O (~ 2 versus ~ 1 wt.%), lower CaO (~ 14 versus ~ 18 wt.%), and slightly lower Mg# (~ 0.82 versus ~ 0.88; La Tourette and Burnett, 1992; Beattie, 1993a,b; Hauri et al., 1994; Wood et al., 1999).

Garnet compositions in our experiments, likewise, are similar to those from the melting experiments of Hirschmann et al. (2003), although with slightly higher Al_2O_3 (24.2 ± 0.2 versus 23.0 ± 0.2) and slightly lower CaO (5.7 ± 0.1 versus 6.0 ± 0.1 wt.%) and Mg# (0.734 ± 0.001

Table 3
Experimentally determined mineral-melt partition coefficients

| | PX21f-4 | | PX21f-5 | PX21f-17 | | PX21g-2 | | PX21h-2 | |
| | 1440 °C, 120 h | | 1450 °C, 144 h | 1440 °C, 72 h | | 1420 °C, 48 h | | 1420 °C, 48 h | |
	Cpx	Gt	Cpx	Cpx	Sp	Cpx	Sp	Cpx	Sp
Li	–	–	–	–	–	0.22(4) [a]	0.13	–	–
Be	–	–	–	–	–	0.024(3)	0.10	–	–
B	–	–	–	–	–	–	–	0.19(9)	0.10
V	–	–	–	–	–	–	–	1.1(2)	1.3
Cr	–	–	–	–	–	–	–	2.8(5)	3.43(8)
Rb	–	–	–	–	–	0.015(2)	0.029	–	–
Sr	–	–	–	–	–	0.067(3)	0.0047	–	–
Y	–	–	–	–	–	–	–	0.37(6)	0.002(1)
Zr	–	–	–	–	–	–	–	0.09(1)	0.0081(9)
Nb	–	–	–	–	–	–	–	0.0029(8)	0.0006(2)
Ba	–	–	–	–	–	–	–	0.005(2)	0.0006(4)
La	–	–	–	–	–	–	–	0.034(6)	0.0002(1)
Nd	–	–	–	–	–	0.24(1)	0.24	–	–
Sm	–	–	–	–	–	0.31(2)	0.18	–	–
Lu	–	–	–	–	–	–	–	0.38(6)	0.0007(4)
Hf	–	–	–	–	–	–	–	0.13(3)	0.003(2)
Ta	–	–	–	–	–	–	–	0.008(2)	0.0004(1)
Pb	–	–	–	–	–	–	–	0.2(1)	0.0005(2)
Th	0.015(2)	0.0032(4)	0.0083(6)	0.015(1)	0.010(3)	0.020(2)	0.016	–	–
U	0.017(2)	0.013(2)	0.0094(6)	0.016(1)	0.014(5)	0.024(2)	0.046	–	–

[a] Numbers in parentheses indicate one standard error uncertainties in terms of least units cited.

versus 0.806±0.001). Compared with existing eclogite melting and U and Th partitioning experiments, the Gt from our experiments have relatively low TiO_2 (0.55±0.03 versus ~1 wt.%) and CaO (5.7±0.1 versus ~8 wt.%), and high Al_2O_3 (24.2±0.2 versus ~23 wt.%) and Mg# (0.734±0.001 versus ~0.61; Pertermann et al., 2004). Our Gt crystals have higher Al_2O_3 (24.2±0.2 versus ~23 wt.%) and CaO (5.7±0.1 versus ~4 wt.%) and lower Mg# (0.734±0.001 versus ~0.88; Salters and Longhi, 1999; Salters et al., 2002) than Gt from peridotite melting experiments. Uranium and Th partitioning experiments conducted on near-liquidus basalts have Gt with higher Al_2O_3 (~26 versus 24.2±0.2 wt.%) and slightly higher Mg# (~0.76 versus 0.734±0.001) than ours (Beattie, 1993a,b; La Tourette et al., 1993; Hauri et al., 1994).

The partition coefficients determined in this study are reported in Table 3. In Fig. 1, we show how Cpx-melt partition coefficients for U increase monotonically from 0.0094±0.0006 at 1450 °C to 0.024±0.002 at 1420 °C, while $D_{Th}^{Cpx/Melt}$ increases from 0.0083±0.0006 to 0.020±0.002 over the same temperature range. The $D_{Th}^{Cpx/Melt}/D_{U}^{Cpx/Melt}$ ratios in our experiments are slightly less than 1, and, with a mean value of 0.88±0.05, do not vary significantly with temperature. The $D_{Th}^{Gt/Melt}$ value determined from our experiment at 1440 °C is 0.0032±0.0004, nearly a factor of 5 smaller than $D_{Th}^{Cpx/Melt}$ (0.015±0.002) at the same conditions, whereas $D_{U}^{Gt/Melt}$ (0.013±0.002) is only slightly smaller than $D_{U}^{Cpx/Melt}$ (0.017±0.002). Our experiments therefore show that $D_{Th}^{Gt/Melt}/D_{U}^{Gt/Melt}$ (0.25±0.04) is much smaller than $D_{Th}^{Cpx/Melt}/D_{U}^{Cpx/Melt}$ during garnet pyroxenite partial melting, confirming that Gt is much more effective at producing ^{230}Th excesses.

Clinopyroxene-melt partition coefficients determined at 2.5 GPa and 1420 °C are presented in Fig. 2, in order of compatibility during peridotite partial melting (Hofmann, 1988), together with partitioning data for partial melting of both eclogites (Pertermann and Hirschmann, 2002; Pertermann et al., 2004) and peridotites (Salters and Longhi, 1999) for comparison. Our $D_i^{Cpx/Melt}$ values are overall similar to those measured in previous studies, suggesting that the variations in Cpx composition discussed above do not produce significant changes in compatibility for most trace elements, though $D_U^{Cpx/Melt}$ and $D_{Th}^{Cpx/Melt}$, which are lower in eclogites, represent an exception to this.

3.2. Approach to equilibrium

The approach to equilibrium for experimental results in this study was evaluated by carrying out experiments
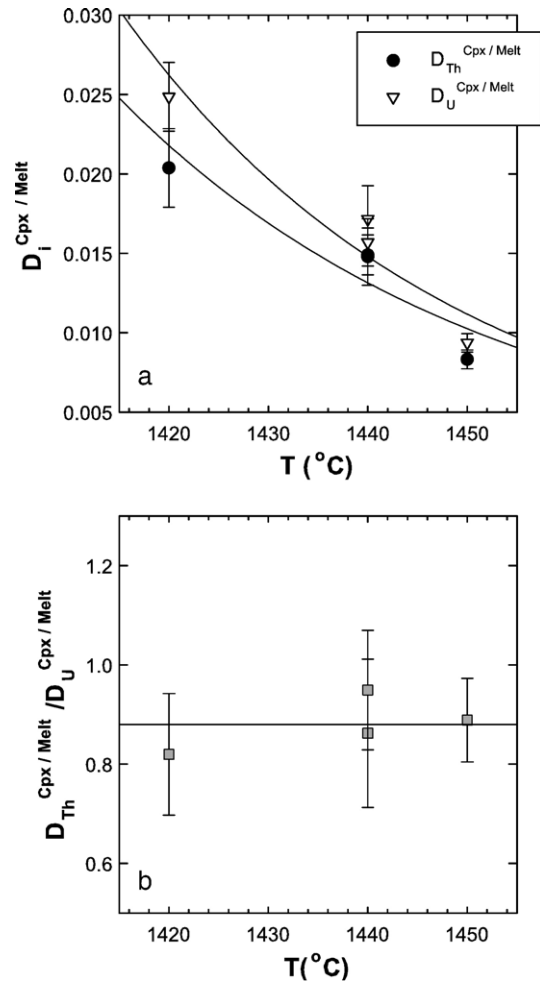

Fig. 1. Temperature vs. (a) $D_i^{Cpx/Melt}$ and (b) $D_{Th}^{Cpx/Melt}/D_{U}^{Cpx/Melt}$ ratio diagrams, showing measured values from experiments PX21f-4, PX21f-5, PX21f-17, and PX21g-2. Plotted lines show (a) Arrhenius relationships between temperature and partition coefficients and (b) the mean $D_{Th}^{Cpx/Melt}/D_{U}^{Cpx/Melt}$ value, demonstrating that while $D_i^{Cpx/Melt}$ values decrease with T, $D_{Th}^{Cpx/Melt}/D_{U}^{Cpx/Melt}$ ratios are relatively constant.

in which the final equilibrium state was approached from two different starting conditions, to demonstrate that the final equilibrium is independent of path. An experiment in which the final pressure–temperature conditions (1440 °C, 2.5 GPa) were approached starting from ambient conditions produced a mineral assemblage of Cpx+Gt+Sp with $D_U^{Cpx/Melt}$=0.017±0.002 and $D_{Th}^{Cpx/Melt}$=0.015±0.002. A second experiment was conducted at 2.5 GPa in which the charge was initially held at 1340 °C for 6 h, then heated at 1 °C/s to 1440 °C and held for 72 h. This experiment produced a mineral assemblage of Cpx+Sp, with $D_U^{Cpx/Melt}$=0.016±0.002 and $D_{Th}^{Cpx/Melt}$=0.015±0.001. The Fe/Mg exchange coefficients for Cpx and melt for these experiments are the same within analytical
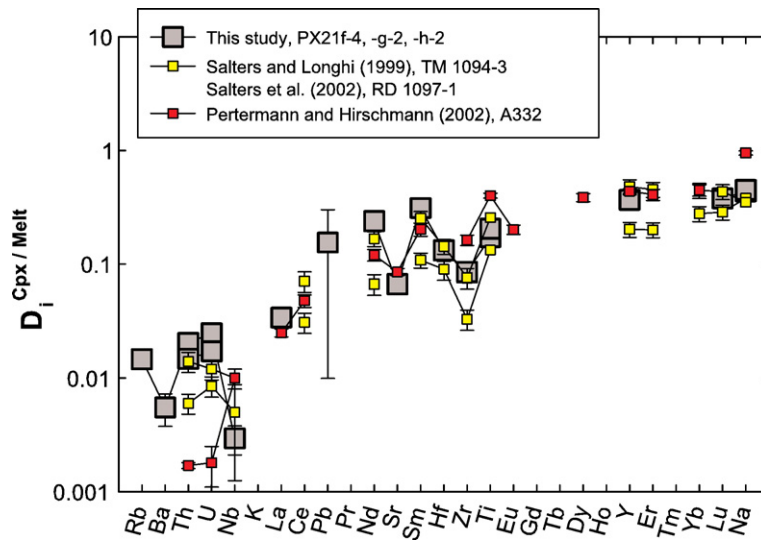
Fig. 2. Spider diagram showing combined Cpx-melt partition coefficients from experiments PX21g-2 and PX21h-2, in order of increasing compatibility (Hofmann, 1988). Data from Pertermann and Hirschmann (2002), Salters and Longhi (1999), and Salters et al. (2002) are shown for comparison between our experiments and eclogite and peridotite partitioning data from the literature. Note that the element ordering of Hofmann (1988) has been retained even for cases where no partitioning data are available in order to avoid the appearance of apparent compatibility anomalies.

uncertainty (0.315±0.004 versus 0.306±0.007). Therefore, while the absence of Gt in the second experiment indicates that an equilibrium mineral assemblage was not achieved, the experimental duration was adequate to attain equilibrium element distribution between minerals and melts.

3.3. Henry's law

In order to analyze the experimental products by SIMS, it was necessary to dope the starting compositions at levels significantly higher than those found in natural basalts. Previous trace element partitioning studies have demonstrated adherence to Henry's Law at concentration levels ranging from 100 ppm to as high as 2 wt.% (Grutzeck et al., 1974; Nicholls and Harris, 1980; Ray et al., 1983; Gallahan and Nielsen, 1992). The total trace element contents of our silicate melts (∼1 wt.%) fall well below the expected upper limit for Henry's law, such that no deviation from Henrian behavior is expected. While we did not carry out an explicit test of Henry's law, there are no systematic differences among experiments carried out using different concentrations of U and Th, and our partition coefficients are in general agreement with literature values determined over a range of doping levels. On the basis of these comparisons, we conclude that our experiments were carried out at concentration levels within the range of Henrian behavior and that our results are appropriate for modeling natural systems.

4. Discussion

4.1. Partitioning of U and Th during partial melting of garnet pyroxenite

The equilibrium partitioning of incompatible trace elements such as U and Th during partial melting is governed at equilibrium by the equivalence of chemical potentials. Because of this, $D_i^{Mineral/Melt}$ values depend on both the pressure–temperature conditions at which partial melting takes place and the compositions of both the minerals in the source rock and the partial melt. As noted in the introduction, there is isotopic evidence to suggest that heterogeneity exists in the source region of OIB (Zindler and Hart, 1986), it is plausible that lithologic heterogeneity is also present and may be a source for enriched lavas (Hirschmann and Stolper, 1996; Lundstrom et al., 1999), and silica-poor garnet pyroxenite is a viable source rock for producing the major element composition of alkaline OIB lavas (Hirschmann et al., 2003; Kogiso et al., 2003, 2004). Melting of garnet pyroxenite begins at higher pressures and temperatures than peridotite, and the compositions of both Cpx and Gt in pyroxenite are different than in lherzolite. These factors have the potential to produce differences in both the absolute and the relative compatibilities of U and Th during partial melting that could create identifiable differences in secular disequilibria patterns in melts. Here we use results from our partitioning experiments to quantify the influence
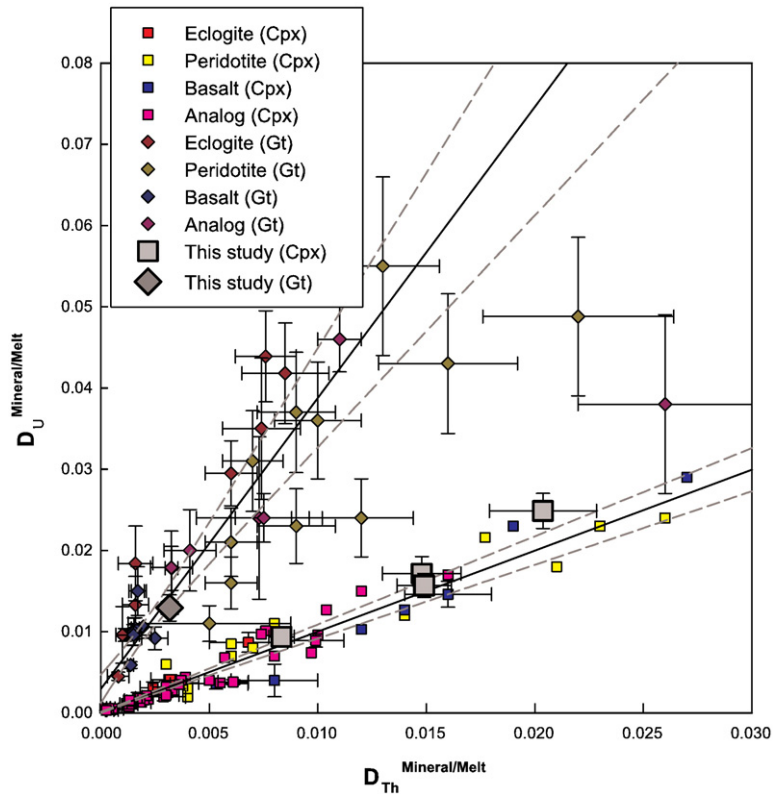
Fig. 3. $D_{Th}^{Mineral/Melt}$ vs. $D_{U}^{Mineral/Melt}$ for Cpx and Gt data from this study and from the literature (Benjamin et al., 1980; La Tourette and Burnett, 1992; Beattie, 1993a,b; La Tourette et al., 1993; Hauri et al., 1994; Lundstrom et al., 1994; Salters and Longhi, 1999; van Westrenen et al., 1999; Wood et al., 1999; van Westrenen et al., 2000; Landwehr et al., 2001; Pertermann and Hirschmann, 2002; Salters et al., 2002; McDade et al., 2003; Pertermann et al., 2004), filtered to show only those experiments with oxygen fugacity at least 1 log unit more reduced than the fayalite–magnetite–quartz buffer (to avoid concerns regarding the effect of U^{6+} on $D_{U}^{Mineral/Melt}$). Error bars show one-sigma standard errors where available (only one-sigma standard deviations were available from Benjamin et al. (1980) and McDade et al. (2003), and only estimated uncertainties were available from Salters and Longhi (1999) and Salters et al. (2002)). Results from double error regressions (solid lines) and 95% confidence envelopes (dashed lines) for Cpx and Gt are shown. Although all data are shown, only $D_{i}^{Mineral/Melt}$ values with reported errors are included in the regressions. The Gt trend follows a steeper slope than the Cpx data, as discussed in Section 4.1 of the text.

of some of these factors on $D_{Th}^{Mineral/Melt}$, $D_{U}^{Mineral/Melt}$, and $D_{Th}^{Mineral/Melt}/D_{U}^{Mineral/Melt}$ ratios during partial melting of garnet pyroxenite. While the composition of the melt can also influence the magnitude of $D_{i}^{Mineral/Melt}$, it is unlikely to change relative compatibilities of isovalent cations with the same charge and similar cationic radii (e.g. Landwehr et al., 2001; Gaetani, 2004).

Given that U^{4+} and Th^{4+} have the same valence state at oxygen fugacity conditions thought to be prevalent in the upper mantle, the variable most likely to influence the relative compatibilities of these elements during partial melting is the size of the lattice site onto which they substitute. Wood et al. (1999) pointed out that for spinel lherzolite of a given bulk composition, Cpx becomes increasingly poorer in Ca^{2+} and richer in Al^{3+} with increasing pressure along the peridotite solidus, and that this likely results in a decrease in the mean size of the Cpx M2 site (designated as r_0 in the lattice strain equation of Blundy

and Wood (1994)). Because the cationic radius of U^{4+} (1.00 Å) is slightly less than that of Th^{4+} (1.05 Å) in VIII-fold coordination (Shannon, 1976), this compositional change should produce a progressive decrease in the compatibility of Th^{4+} relative to U^{4+} in spinel lherzolite with increasing depth in the upper mantle. Landwehr et al. (2001) experimentally demonstrated the influence of Cpx composition on $D_{Th}^{Cpx/Melt}/D_{U}^{Cpx/Melt}$ in the simplified system $CaO–MgO–Al_2O_3–SiO_2–Na_2O$, producing $D_{Th}^{Cpx/Melt}/D_{U}^{Cpx/Melt}$ ratios ranging from 1.64 ± 0.14 for relatively CaO-rich (23.08 ± 0.19 wt.%), Al_2O_3-poor (1.27 ± 0.04 wt.%) Cpx with $r_0=1.031$ Å, to 0.58 ± 0.11 for a CaO-poor (6.3 ± 0.3 wt.%), Al_2O_3-rich (19.5 ± 0.4 wt.%) Cpx with $r_0=0.952$ Å.

To evaluate the possibility that Cpx and Gt compositional differences related to differing lithologies also cause systematic differences in U/Th fractionation
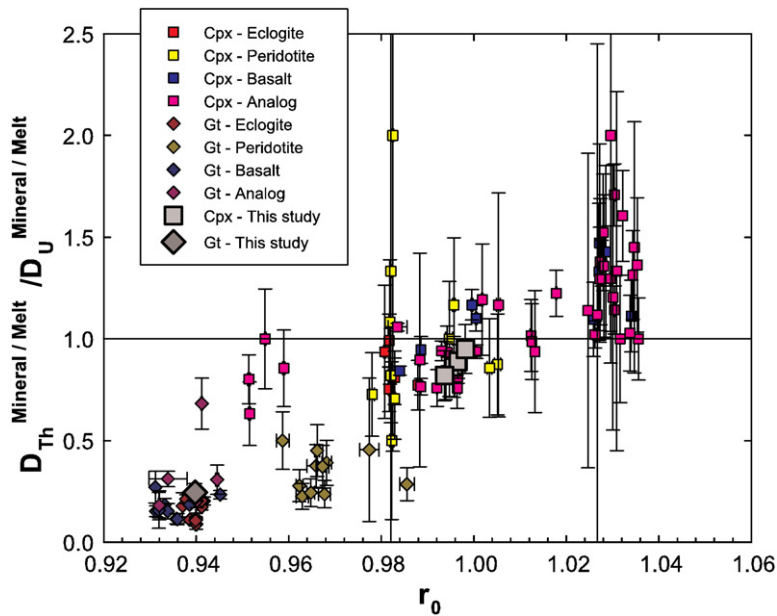
Fig. 4. Plot showing relationships between calculated r_0 values and $D_{Th}^{Mineral/Melt}/D_U^{Mineral/Melt}$ ratios for both Cpx and Gt; data set and error bars as in Fig. 3. Note that for a given r_0 value $D_{Th}^{Mineral/Melt}/D_U^{Mineral/Melt}$ ratios are significantly lower for Gt than for Cpx.

during partial melting, we compared U and Th partition coefficients determined for Cpx and Gt from our experiments with those determined in previous studies for partial melting of eclogite and peridotite and from near-liquidus experiments on basalts (Figs. 3 and 4). The nominal radii (r_0) of the Cpx M2 and Gt X lattice sites were calculated as a function of mineral composition for our partitioning experiments and those from the literature using Equation 15 of Wood and Blundy (1997) and Equation 2 of van Westrenen et al. (2001), respectively. Applying these values to understand the geochemical behavior of U^{4+} and Th^{4+} requires the assumption that $r_0^{3+} = r_0^{4+}$, but the uncertainty involved with this approximation is small (e.g. (Wood et al., 1999; Landwehr et al., 2001; Blundy and Wood, 2003).

There are no obvious correlations between r_0 and $D_{Th}^{Mineral/Melt}$ or $D_U^{Mineral/Melt}$ for either Cpx or Gt. This is not surprising, given that the magnitudes of both partition coefficients depend upon pressure, temperature, and melt composition in addition to mineral composition. However, there are statistically significant correlations between $D_{Th}^{Mineral/Melt}$ and $D_U^{Mineral/Melt}$ for both Cpx and Gt, with an especially strong relationship for Cpx (Fig. 3):

$$D_U^{Cpx/Melt} = 1.0 \pm 0.9 \times D_{Th}^{Cpx/Melt} + 0.00006 \pm 0.00008 \quad (1)$$

$$D_U^{Gt/Melt} = 3.6 \pm 0.7 \times D_{Th}^{Gt/Melt} + 0.0030 \pm 0.0017 \quad (2)$$

where stated uncertainties are 2σ. For Cpx, the slope of this correlation is 1.0, reflecting the small variation around a value of 1 exhibited by the $D_{Th}^{Cpx/Melt}/D_U^{Cpx/Melt}$ ratio. As the individual compatibilities of U and Th in Cpx increase, their relative compatibilities do not change significantly. In the case of Gt, $D_U^{Gt/Melt}$ increases approximately 4 times faster than $D_{Th}^{Gt/Melt}$, so that the $D_{Th}^{Gt/Melt}/D_U^{Gt/Melt}$ ratio is typically ~0.25 (note that Eq. (2) has a non-zero intercept, an indication that this relationship is likely to be curved). There appears to be no systematic change in compatibility of either U or Th among the different lithologies (pyroxenite, eclogite, or peridotite) for Cpx. This may not be true for Gt, however, where U^{4+} and Th^{4+} appear to be more compatible during partial melting of peridotite relative to eclogite or pyroxenite.

Fig. 4 is a plot of r_0 versus $D_{Th}^{Mineral/Melt}/D_U^{Mineral/Melt}$ ratio for experimentally produced Cpx and Gt. From this comparison it can be seen that the $D_{Th}^{Mineral/Melt}/D_U^{Mineral/Melt}$ ratio increases systematically with increasing r_0, as suggested for Cpx by Wood et al. (1999), and that this increase can be driven by bulk composition as well as variations in pressure–temperature conditions. For Cpx, the relative compatibilities of U and Th switch at an r_0 value ~1.00 Å, comparable to the cationic radius of U^{4+}. Clinopyroxenes produced in our experiments are characterized by a narrow range of r_0 values (0.994–0.998 Å) that fall near the middle of the overall range for Cpx from partitioning experiments (0.951 to

1.036 Å; Fig. 4), and a mean $D_{Th}^{Cpx/Melt}/D_{U}^{Cpx/Melt}$ ratio of 0.88 ± 0.05. Clinopyroxenes with compositions relevant to eclogite partial melting have M2 lattice sites with r_0 from 0.981 to 0.988 Å, significantly smaller than for Cpx from silica-poor garnet pyroxenite, and are characterized by $D_{Th}^{Cpx/Melt}/D_{U}^{Cpx/Melt}$ ratios of 0.77 to 1.00. Clinopyroxene from experiments carried out to investigate partitioning during peridotite partial melting have r_0 values from 0.978 to 1.005 Å, and $D_{Th}^{Cpx/Melt}/D_{U}^{Cpx/Melt}$ ratios of 0.50 to 2.0. These are substantially broader ranges than for either pyroxenite or eclogite Cpx and may, in part, reflect the broader range of pressure–temperature conditions of these experiments. Clinopyroxene from partitioning experiments on near-liquidus basalts have the widest range of r_0 values (0.984 to 1.030 Å), with $D_{Th}^{Cpx/Melt}/D_{U}^{Cpx/Melt}$ ratios of 0.83 to 2.0, and define the upper end of the range for experiments on "natural" starting compositions. This is likely a reflection of their systematically higher CaO contents.

The r_0 values calculated for the Gt X site are smaller than the majority of those for the Cpx M2 site, with a narrower range of values (0.931 to 0.986 Å). The $D_{Th}^{Gt/Melt}/D_{U}^{Gt/Melt}$ ratios are always much less than one (0.09–0.68 with a mean of 0.25). Garnets from pyroxenite melt (r_0 = 0.940 Å; $D_{Th}^{Gt/Melt}/D_{U}^{Gt/Melt}$ = 0.245), eclogite melt (r_0 = 0.937 to 0.942 Å; $D_{Th}^{Gt/Melt}/D_{U}^{Gt/Melt}$ = 0.087–0.211), and near-liquidus basalt (r_0 = 0.931 to 0.945 Å; $D_{Th}^{Gt/Melt}/D_{U}^{Gt/Melt}$ = 0.113–0.271) partitioning experiments have r_0 values and $D_{Th}^{Gt/Melt}/D_{U}^{Gt/Melt}$ ratios comparable to one another. The r_0 values for Gt from experiments relevant to peridotite partial melting are significantly larger than for mafic lithologies, ranging from 0.959 to 0.986 Å, and $D_{Th}^{Gt/Melt}/D_{U}^{Gt/Melt}$ ratios (0.226 to 0.500) that tend to be larger. Therefore, as with Cpx, Gt in mafic lithologies tend to produce large [230]Th excesses relative to peridotite.

In summary, the relationships shown in Figs. 3 and 4 strongly support the contention that, although other factors also contribute, the principal control on the relative compatibilities of U and Th during partial melting is the size of the VIII-fold lattice sites in both Cpx and Gt. The size of the Cpx M2 site and of the Gt X site in eclogite and pyroxenite tend to be small relative to peridotite, such that bulk rock D_{Th}/D_{U} ratios will tend to be higher. Therefore, for a given melting rate and extent of partial melting, mafic lithologies tend to produce larger [230]Th excesses than peridotites. As discussed in the next section, this effect is damped by the greater overall extents of partial melting experienced by eclogites and pyroxenites relative to peridotite.

4.2. Uranium series constraints on the role of garnet pyroxenite in the generation of alkaline OIB

Ocean island basalt lavas are characterized by a broad spectrum of trace element and isotopic compositions. Zindler and Hart (1986) and others have identified a variety of mantle components that mix to produce OIB globally. These components consist of a depleted end member, hypothesized to be the ambient depleted MORB mantle (DMM), and several distinct enriched components (EMI, EMII) characterized by time-integrated incompatible trace element enrichment as evidenced by their long-lived radiogenic isotopic signatures.

The lithologic identity of the enriched component in the OIB source is hotly debated. Some studies suggest that the enriched signal is produced by cryptically-metasomatized ambient mantle peridotite (e.g. Workman et al., 2006), while others hypothesize that a mafic/eclogitic source is responsible for this enrichment (e.g. Hirschmann and Stolper, 1996; Sobolev, 2000; Hirschmann et al., 2003). Because U–Th elemental fractionation is particularly sensitive to both mineral composition and the modal abundance of Gt in a lava's mantle source, measurements of ([230]Th/[238]U) disequilibria in OIBs provide an important means to address the question of source lithology.

Previously, Stracke et al. (1999) suggested that, on the basis of existing experimentally determined partition coefficients for U and Th, partial melting of a mafic mantle lithology (e.g. pyroxenite, eclogite) could not generate significant degrees of [230]Th excess in lavas. Their ([230]Th/[238]U) values for pyroxenite melting were calculated using partitioning data from Hauri et al. (1994) with bulk D_{Th}/D_{U} = 0.96 for pyroxenite and 0.83 for eclogite. These bulk partition coefficients generate only 5–20% [230]Th excess, whereas the Salters and Longhi (1999) D values for U and Th used by Stracke et al. (1999) bulk D_{U}/D_{Th} ∼ 2) could generate up to ∼ 100% [230]Th excess during partial melting of peridotite. While their use of the Salters and Longhi (1999) partition coefficients for peridotite could produce the necessary large [230]Th excesses, the $D_i^{Mineral/Melt}$ values they used for pyroxenite from Hauri et al. (1994) came from experiments on near-liquidus basalt. While the $D_{Th}^{Gt/Melt}/D_{U}^{Gt/Melt}$ ratio from these experiments is comparable to pyroxenite (0.233 vs. 0.245), the $D_{Th}^{Cpx/Melt}/D_{U}^{Cpx/Melt}$ ratio is significantly higher (1.13 ± 0.03 vs. 0.88 ± 0.05), leading to [230]Th excesses that are too small. Therefore, they are not applicable to such an assessment.

The partition coefficients determined from our experiments are specific to partial melting of garnet
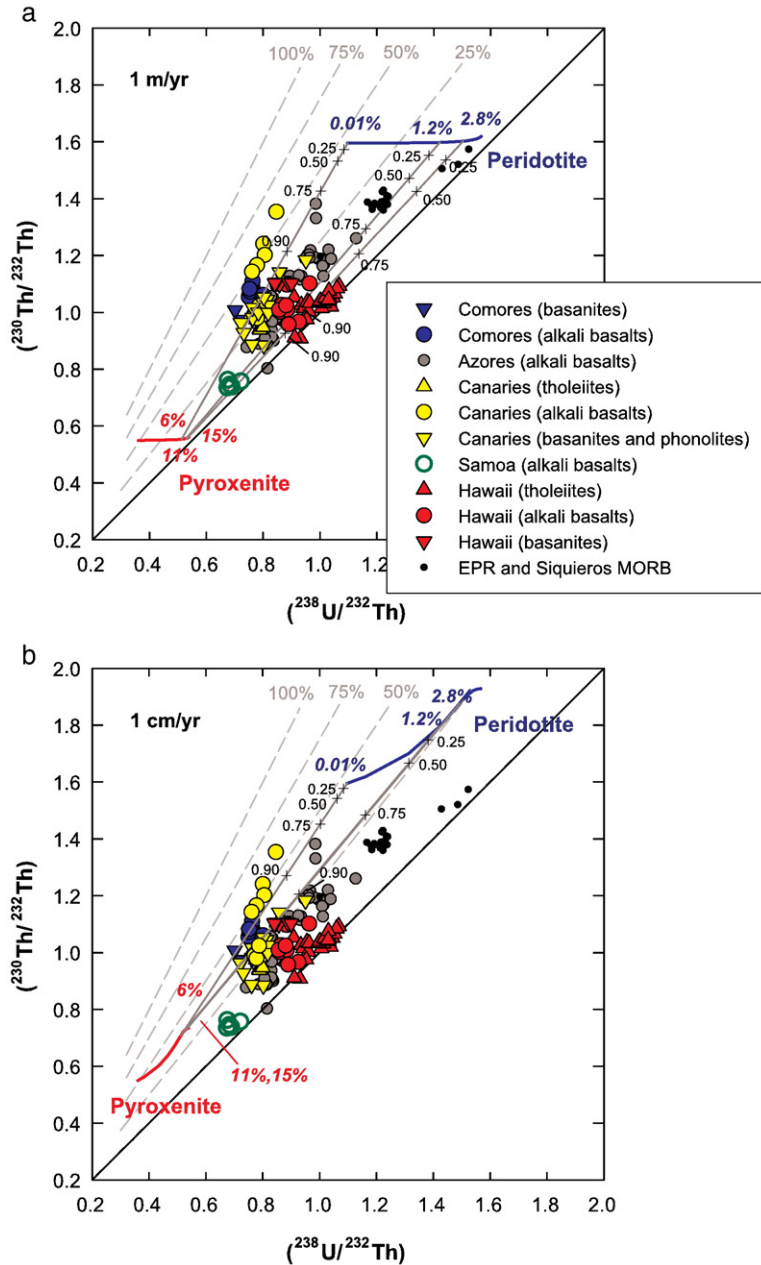
Fig. 5. (^{238}U/^{232}Th) vs. (^{230}Th/^{232}Th) equiline diagram for upwelling rates of (a) 1 m/yr and (b) 1 cm/yr, showing chromatographic melting trajectories with residual porosities of 0.5% and binary mixing trends described in Section 4.2 of the text and the Appendix A. The curves labeled "Peridotite" and "Pyroxenite" show the progressive melting paths from each of those source lithologies, and the dark gray lines show mixing trends between melts of peridotitic (blue) and pyroxenitic (red) source lithologies at melt fractions reflecting the different depths to the solidii and productivities during upwelling. Tick or plus marks with labels show the fraction of pyroxenite in the binary pyroxenite–peridotite mixtures; note, however, that the precise position of these ticks is dependent on our choice of endmember values. Data from OIB rocks from Hawaii (Cohen and O'Nions, 1993; Sims et al., 1995; Cohen et al., 1996; Pickett and Murrell, 1997; Pietruszka, 1999; Sims et al., 1999), Samoa (Sims and Hart, 2006; Sims et al., in press), the Canaries (Sigmarsson et al., 1998; Lundstrom et al., 2003), the Azores (Turner et al., 1997; Widom et al., 1997; Claude-Ivanaj et al., 2001; Bourdon et al., 2005), and the Comores (Bourdon et al., 1998; Claude-Ivanaj et al., 1998) are plotted for comparison, together with East Pacific Rise (EPR) and Siquieros data (Lundstrom et al., 1999; Sims et al., 1999). Also shown for comparison are light gray dashed lines with labels indicating constant ^{230}Th excess. Note that because of the slopes of these lines, the enriched pyroxenitic source reaches higher values of ^{230}Th excess than the depleted peridotitic source.

pyroxenite and thus provide an important test of its effect on (^{230}Th/^{238}U) disequilibria formed during OIB genesis. Here we use our partitioning data to evaluate the role of mixing of peridotite and garnet pyroxenite melts in generating the U–Th, Sm–Nd, and Nd isotope systematics of OIB. In our calculations we consider the differences in productivities (Hirschmann and Stolper, 1996) of these two lithologic end member components (Fig. 5). Because of the short half-life of ^{230}Th (75.4 ka) relative to the timescales of melt generation and magma transport we also consider the effects of ^{230}Th ingrowth during the melt generation process using an analytic approximation (Sims et al., 1999) to the 1-dimensional chromatographic melting model of Spiegelman and Elliott (1993). The main parameters of our melting-mixing models are: (1) $D_i^{\mathrm{Mineral/Melt}}$ values, (2) melt fraction, (3) solid mantle upwelling rate, (4) porosity of the melting region, and (5) mixing proportions (a detailed description of our melting/mixing calculations can be found in the supplemental information).

In contrast with the results of Stracke et al. (1999), calculations carried out using our new partition coefficients show that at the limit of melting (when F approaches zero) a garnet pyroxenite source generates slightly larger ^{230}Th excesses (52%) than peridotite melting (46%) using $D_{\mathrm{Th}}^{\mathrm{Mineral/Melt}}$ and $D_{\mathrm{U}}^{\mathrm{Mineral/Melt}}$ values from Salters et al. (2002) (see Table 2 in the Appendix for $D_i^{\mathrm{Mineral/Melt}}$ values and modes used). At slower upwelling rates (1 cm/yr), (^{230}Th/^{238}U) disequilibria are maintained or even enhanced over the duration of upwelling because of ^{230}Th ingrowth (Fig. 5b), whereas for faster upwelling (1 m/yr), the degree of melting exerts a stronger control over the amount of disequilibria generated (Fig. 5a). Because of the larger buoyancy flux beneath ocean islands like Hawaii, fast upwelling is more appropriate, and indeed several studies have now shown that U–Th disequilibria and U–Pa disequilibria in places like Hawaii can be described by time independent melting models (Sims et al., 1995; Elliott, 1997; Sims et al., 1999; Bourdon and Sims, 2003).

Using our understanding of relative melt productivities for the two lithologies and conservative estimates for productivity (Langmuir et al., 1992; Hirschmann and Stolper, 1996; Hirschmann et al., 1999; Asimow et al., 2001; Pertermann and Hirschmann, 2003), mixing trends were calculated between melt fractions for pyroxenite and peridotite that reflect the differences in onset of melting and relative productivities. When the large productivity predicted for mafic lithologies relative to peridotite is taken into account, the resulting mixing lines, shown in Fig. 5a, can explain a majority of the alkali OIB data (only

the Canaries and Comores data require greater disequilibria than are generated by our model). The most enriched samples (i.e. Samoa) show small and uniform ^{230}Th excesses, while more depleted lavas (like MORB) have large and highly variable ^{230}Th excesses (e.g. Sims and Hart, 2006). While, in principle, the alkaline OIB data in Fig. 5 are consistent with partial melting of a mixed pyroxenite–peridotite mantle source lithology, it is important to note that the data could be equally well explained by binary mixing of melts from two peridotite sources with different isotopic and trace element signatures (i.e. mixing of partial melts from a 'normal' peridotitic source with those from a metasomatically enriched peridotite source).

Comparison of U–Th disequilibria with other trace element fractionations provides more definitive constraints on both melting processes and source lithologies. In Fig. 6 we compare U–Th disequilibria with the parameter $\alpha_{\mathrm{Sm-Nd}}$ for several suites of oceanic basalts (where $\alpha_{\mathrm{Sm-Nd}} = (\mathrm{Sm/Nd})_{\mathrm{lava}}/(\mathrm{Sm/Nd})_{\mathrm{source}}$,
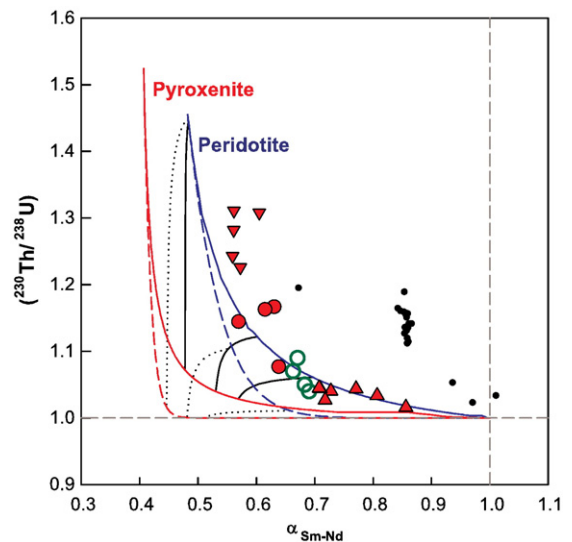

Fig. 6. $\alpha_{\mathrm{Sm-Nd}}$ vs. (^{230}Th/^{238}U) (a) batch (solid) and fractional (dashed) melting trajectories for peridotite (blue line) and pyroxenite (red line), with binary peridotite–pyroxenite mixing trends shown as thin solid black (for batch melting) and dotted black (fractional) lines. Melt fractions for mixing are the same as in Fig. 5, as are symbols for Hawaii (Cohen and O'Nions, 1993; Sims et al., 1995; Cohen et al., 1996; Pickett and Murrell, 1997; Pietruszka, 1999; Sims et al., 1999), Samoa (Sims et al., 1999; Sims and Hart, 2006; Sims et al., in press), and MORB data (Lundstrom et al., 1999; Sims et al., 1999). Sm and Nd $D_i^{\mathrm{Gt/Melt}}$ values are calculated as described in the text and supplemental information. The significantly reduced number of data points shown here relative to Fig. 5 reflects the smaller number of samples for which comprehensive U–Th disequilibrium, Sm and Nd concentration, and Nd isotope data sets exist.

and (Sm/Nd)$_{source}$ is calculated using the sample's $^{143}Nd/^{144}Nd$ ratio and a 1.8 Ga model age (see e.g. DePaolo, 1988; Sims et al., 1995)). This approach has been previously used to constrain melting processes in Hawaii (Sims et al., 1995; Elliott, 1997; Sims et al., 1999; Stracke et al., 1999), Samoa (Sims and Hart, 2006; Sims et al., in press), and the East Pacific Rise (Sims et al., 2002). While our new data provide constraints on U and Th partitioning, due to the nucleation difficulties associated with Gt, our experiments lack $D_i^{Garnet/Melt}$ values for Sm and Nd. Thus, in order to examine silica-poor garnet pyroxenite melting for these systems, we apply our measured $D_i^{Cpx/Melt}$ values for Th, U, Sm, and Nd, while our measured $D_i^{Gt/Melt}$ values for Th and U are supplemented by $D_{Sm}^{Gt/Melt}$ and $D_{Nd}^{Gt/Melt}$ values calculated for our pyroxenitic Gt compositions using the lattice strain model of van Westrenen et al. (2001) and Draper and van Westrenen (2007). Using these partitioning constraints and published partitioning data for peridotite (Salters et al., 2002), and applying them to forward batch and fractional melting, we find that existing Hawaii and Samoa data plot closer to the peridotite batch melting trend than that for pyroxenite or to fractional melting trends (Fig. 6). We also note, as has been found in previous OIB studies (e.g. Sims et al., 1995; Elliott, 1997; Sims et al., 1999), that the Hawaiian OIB data closely follow a batch melting trend and that Th/U and Sm/Nd fractionations are coupled, with the largest extents of Th/U and Sm/Nd fractionation occurring in the alkali basalts and basanites (inferred to be derived by low extents of melting) and the least extents of Th/U and Sm/Nd fractionation occurring in the tholeiites (inferred to be the largest melt fractions). As discussed above, this is because the inferred fast solid mantle upwelling rates beneath Hawaii do not allow for significant ^{230}Th ingrowth in the melting column, and the range in the extent of melting is large (i.e. from tholeiites to basanites), such that the degree of melting exerts a dominant control on the extent of fractionation for both U–Th and Sm–Nd. Conversely, MORB data, shown for comparison, do not lie on this trend (Fig. 6), having much larger ^{230}Th excesses for a given Sm/Nd, and here ^{230}Th ingrowth is inferred to be important because of the slow upwelling rates beneath MOR.

It is generally assumed that mantle pyroxenite is isotopically distinct and from a source characterized by a long-term incompatible element enrichment. When comparing the Hawaiian lavas' Nd isotopic composition with U–Th disequilibria and Sm/Nd fractionation, Stracke et al. (1999) observed that trends formed by Hawaiian lavas have an opposite slope from what would be
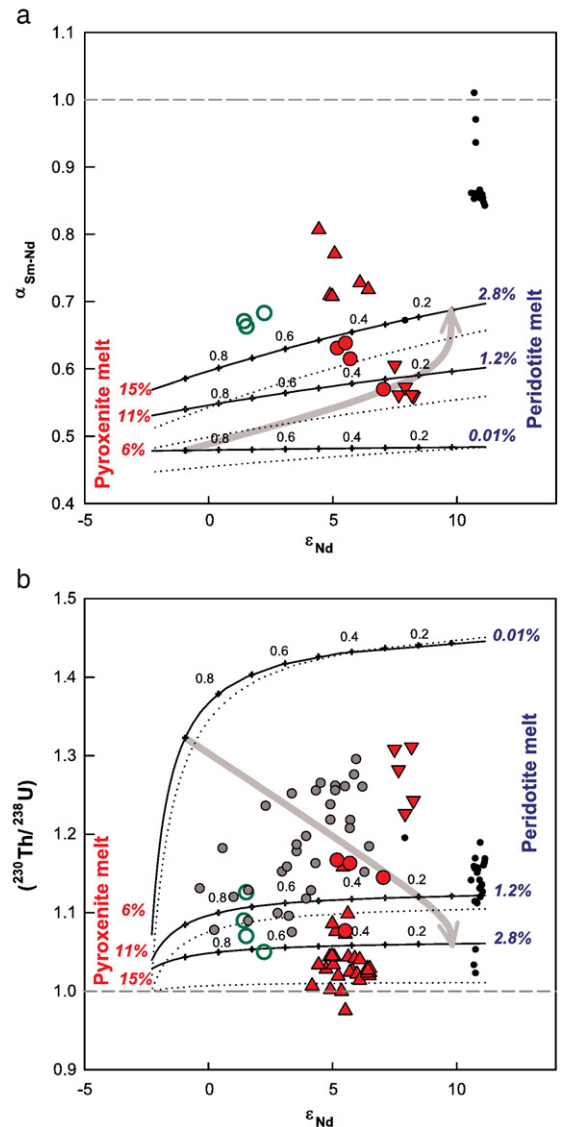

Fig. 7. ε_{Nd} vs. (a) α_{Sm-Nd} and (b) ($^{230}Th/^{238}U$), showing mixing lines for batch (solid) and fractional (dotted) melts of peridotite (blue) and pyroxenite (red) at melting fractions shown in blue and red. As in Fig. 5, tick marks with numbers on the batch melting curves show the fraction of pyroxenite melt in the mixtures. Hawaii (Cohen and O'Nions, 1993; Sims et al., 1995; Cohen et al., 1996; Pickett and Murrell, 1997; Pietruszka, 1999; Sims et al., 1999), Samoa (Sims and Hart, 2006; Sims et al., in press), Azores (Turner et al., 1997; Widom et al., 1997; Claude-Ivanaj et al., 2001; Bourdon et al., 2005), and MORB data (Lundstrom et al., 1999; Sims et al., 1999) are shown for comparison; symbols as in Fig. 5. Light gray arrows show the direction of progressive melting in an upwelling column with ∼2% pyroxenite in the source. Hawaiian, Azores, and Samoan data form a trend counter to what would be expected for progressive melting, as also observed in Stracke et al. (1999).

expected from progressive melting and mixing of melts from two different lithologies in a melting column. Using our new pyroxenitic partition coefficients for U and Th and the calculated values for Sm/Nd described above and in the supplemental material, we find that our model melting and mixing curves give results consistent with the Stracke et al. (1999) predictions. As demonstrated in Fig. 7, the OIB data fall along a trend counter to the direction expected for progressive melting of a source with a fixed quantity of pyroxenite present. As proposed by Stracke et al. (1999), melting a peridotite with enriched signatures, and mixing those melts with melts of a deleted, "normal" peridotite, is an alternative explanation for the trends seen in the Hawaiian, Azores, and Samoan data sets.

5. Conclusions

Previous experimental studies of U and Th partitioning have been conducted for peridotites, eclogites, and basaltic melt compositions, and to this data set we add new measurements for Cpx and Gt co-existing in a silica-poor garnet pyroxenite melt. At 1420–1450 °C and 2.5 GPa, our starting composition PX21, representing a 21% melt of the silica poor garnet pyroxenite MIX1G after Hirschmann et al. (2003), was found to have $D_{Th}^{Cpx/Melt}/D_{U}^{Cpx/Melt}=0.82\pm0.12$ to 0.95 ± 0.12 and $D_{Th}^{Gt/Melt}/D_{U}^{Gt/Melt}=0.25\pm0.04$.

These new data provide a quantitative test for viability of pyroxenite in the mantle source of OIB. Taking into account depth to solidi and variable productivities, we conclude that chromatographic and batch melts of silica-poor garnet pyroxenite and ambient peridotite can mix to generate most of the observed $^{238}U–^{230}Th$ disequilibria. However, Hawaiian, Samoan, and Azores lavas form trends in trace element fractionation vs. radiogenic isotope space with slopes counter to expected progressive melting trends, suggesting that metasomatised peridotite could better explain the inferred isotopic enrichment in the source of these lavas. Further testing with new data from other ocean island settings may help to further constrain the role of garnet pyroxenite in global OIB production.

Acknowledgements

Appendix A

In Section 4.2, we apply the chromatographic melting model of Spiegelman and Elliott (1993) (Fig. 5). Calculations were carried out using our experimentally determined partition coefficient values for garnet pyroxenite partial melting ($D_{Th}^{Cpx/Melt}=0.015$, $D_{U}^{Cpx/Melt}=0.017$, $D_{Th}^{Gt/Melt}=0.0032$, and $D_{U}^{Gt/Melt}=0.013$) and partitioning data from Salters and Longhi (1999) and Salters et al. (2002) for peridotite partial melting ($D_{Th}^{Cpx/Melt}=0.004$, $D_{U}^{Cpx/Melt}=0.003$, $D_{Th}^{Gt/Melt}=0.017$, $D_{U}^{Gt/Melt}=0.038$, $D_{Th}^{Ol/Melt}=0.0005$, $D_{U}^{Ol/Melt}=0.00005$, $D_{Th}^{Opx/Melt}=0.009$, and $D_{U}^{Opx/Melt}=0.008$, where Ol refers to olivine and Opx to orthopyroxene; see Table 2 in the Appendix). We use a porosity of 0.5% and endmember upwelling rates of 1 m/yr and 1 cm/yr to demonstrate the competing effects of upwelling and degree of melting in generating $^{230}Th–^{238}U$ disequilibria, since ingrowth, in addition to U–Th fractionation, accounts for much of the disequilibria produced at low upwelling rates (Sims et al., 1995; Elliott, 1997; Sims et al., 1999; Bourdon et al., 2006). To roughly allow for (1) the larger degrees of melting achieved by pyroxenite and (2) melting to continue slightly beyond the largest melt fractions in our binary mixtures (see below), we assign maximum degrees of melting of 0.1 for the peridotite and 0.2 for the pyroxenite (as shown below. We chose peridotite mineral modes of 8% Cpx, 12% Gt, 59% Ol, and 21% Opx (Table 2 in the Appendix), for parallel comparison with relevant U-series studies such as Sims et al. (1995, 1999).

While other studies have placed eclogite and pyroxenite solidi 12–50 km deeper than the peridotite solidus (Hirschmann and Stolper, 1996; Pertermann and Hirschmann, 2003; Kogiso et al., 2004), Kogiso et al. (2003) determined the MIX1G solidus to be less than 50 °C below the peridotite solidus, which, using typical solidus slopes of 120 °C/GPa for both pyroxenite and peridotite, places the MIX1G solidus only 6.5 km below the onset of peridotite melting.

We estimate that 40% Gt is present in pyroxenite at 3.4 GPa, or 106.5 km depth (6.5 km below the peridotite solidus in a 100 km melting column; see Table 2 in the Appendix for mineral modes) on the basis of previous experimental results for the MIX1g composition. Calculations for pyroxenite mineral modes coexisting with a 19% melt of MIX1g at 5 GPa show a significantly greater abundance of Gt than Cpx (Kogiso et al., 2003). Similar calculations for experiments from Hirschmann

et al. (2003) demonstrate that almost no Gt is present after 14% melting at 2 GPa. Mass balance calculations for the remaining melt in these two experiments suggest that at high pressure, almost 60% Gt is present on the solidus, while at 2 GPa less than 10% is present.

We chose initial ($^{238}U/^{232}Th$) and ($^{230}Th/^{232}Th$) ratios for the pyroxenite endmember component using the non-linear regression of Samoan data in Sims and Hart (2006); Samoan lavas have the most enriched isotopic signatures and lowest ($^{238}U/^{232}Th$) of any OIB (0.6) (Sims and Hart, 2006; Sims et al., submitted for publication), and the Sims and Hart (2006) regression calculates Th/U = 5.1–5.5 for the EM2 endmember component. East Pacific Rise lavas represent some of the most depleted MORB samples with the highest ($^{230}Th/^{232}Th$) and ($^{238}U/^{232}Th$) ratios (Lundstrom et al., 1999; Sims et al., 2002). Thus, for the peridotite endmember we use data from the most extreme EPR sample (with respect to ε_{Nd}; ($^{238}U/^{232}Th$) = 1.6). All sources begin in secular equilibrium.

Previous studies have observed that productivity is low for at least the first 2–3% of melting above the solidus for all compositions (Langmuir et al., 1992; Hirschmann and Stolper, 1996; Hirschmann et al., 1999; Asimow et al., 2001; Pertermann and Hirschmann, 2003). Productivity then increases rapidly with increasing extent of partial melting, until it reaches a maximum at the point of Cpx exhaustion; once Cpx is absent, productivity drops abruptly and climbs again slowly until another phase is exhausted, though productivity is probably low enough after Cpx exhaustion that melting does not proceed far beyond this point. Calculated productivities from Hirschmann et al. (1999) for fertile peridotite melting increase from ∼5%/GPa just above the solidus to ∼24%/GPa at the point of Cpx exhaustion (∼18% melting). Due to their different solidi and melting intervals, pyroxenite experiences this increase at a different rate during upwelling, causing the pyroxenite to melt significantly more. Hirschmann and Stolper (1996) estimated that peridotite initially melts at 0.4%/km and that pyroxenites melt 20–50% faster than this, and diffusive heating below the peridotite solidus generates an additional 0.6–3.9%/km (17–120%/GPa) of melting for pyroxenites (Hirschmann and Stolper, 1996).

Based on studies by Pertermann and Hirschmann (2003) and Kogiso et al. (2003), we estimate that a MIX1G-type pyroxenite, which has a narrow melting interval of ∼100 °C, would melt at a similar rate to eclogite near its solidus (15%/GPa), and that diffusive heating could conservatively add another 15%/GPa of melting. Over 6.5 km of upwelling, these productivities, if constant, would generate 6% melting. Because MELTS can overestimate melting (e.g. Hirschmann et al., 1999),

we use very conservative productivity estimates and suggest that for the next 5 km productivity for the pyroxenite is as low as 20%/GPa. Concurrently, the peridotite begins melting with a near-solidus productivity of 5%/GPa (Hirschmann et al., 1999); thus, after 5 more km of upwelling, pyroxenite has experienced 10.8% melting and peridotite 1.2%. After a further 5 km of upwelling, with a higher pyroxenite productivity of 25%/GPa and peridotite productivity of 10%/GPa, the pyroxenite source has melted 14.8% and the peridotite source 2.8%. Mixing lines based on these calculations are shown and labeled with the respective melt fractions of each mixing melt in Figs. 5–7. Note that step-wise melting in this fashion necessarily underestimates what are probably continuously increasing productivities during upwelling, again making these estimates conservative in terms of each melting lithology's ability to fractionate trace elements during upwelling and melting.

To test the agreement of the U–Th modeling with other isotopic systems, we also applied batch, fractional, and chromatographic melting models to α_{Sm-Nd} (where $\alpha_{Sm-Nd} = (Sm/Nd)_{lava}/(Sm/Nd)_{source}$, and $(Sm/Nd)_{source}$ is calculated using the sample's $^{143}Nd/^{144}Nd$ ratio and a 1.8 Ga model age) during melting of pyroxenite and peridotite (Fig. 6). Partition coefficient data for Sm and Nd are from Salters et al. (2002) for peridotite, and for pyroxenite we use our measurements for Cpx partitioning and calculate Gt partition coefficients from van Westrenen et al. (2001) and Draper and van Westrenen (2007). We chose source Sm and Nd concentrations for the depleted peridotite and enriched pyroxenite sources from the Workman et al. (2004) and Workman and Hart (2005) inversions for the DMM and EM2 endmembers, respectively. Other parameters for melting and mixing are the same as above. In Fig. 7, the same batch and fractional melting and mixing trends for α_{Sm-Nd} and ($^{230}Th/^{238}U$) are plotted against ε_{Nd}.

Appendix B. Supplementary data

References

Armstrong, J.T., 1988. Quantitative analysis of silicate and oxide minerals: comparison of Monte Carlo, ZAF, and $\phi(\rho z)$ procedures. In: Newbury, D.E. (Ed.), Microbeam Analysis – 1988. San Francisco Press, San Francisco, CA, pp. 239–246.

Asimow, P.D., Hirschmann, M.M., Stolper, E.M., 2001. Calculation of peridotite partial melting from thermodynamic models of minerals

and melts. IV. Adiabatic decompression and the composition and mean properties of mid-ocean ridge basalts. J. Petrol. 42, 963–998.

Beattie, P., 1993a. The generation of uranium series disequilibria by partial melting of spinel peridotite; constraints from partitioning studies. Earth Planet. Sci. Lett. 117, 379–391.

Beattie, P., 1993b. Uranium–thorium disequilibria and partitioning on melting of garnet peridotite. Nature 363, 63–65.

Benjamin, T., Heuser, W.R., Burnett, D.S., Seitz, M.G., 1980. Actinide crystal-liquid partitioning for clinopyroxene and Ca3(PO4)2. Geochim. Cosmochim. Acta 44, 1251–1264.

Blundy, J.D., Wood, B.J., 1994. Prediction of crystal-melt partition coefficients from elastic moduli. Nature 372, 452–454.

Blundy, J.D., Wood, B.J., 2003. Mineral-melt partitioning of uranium, thorium, and their daughters. Reviews in Mineralogy, 52, pp. 59–123.

Bourdon, B., Sims, K.W.W., 2003. U-series constraints on intraplate basaltic magmatism. Rev. Mineral. Petrol. 52, 215–254.

Bourdon, B., Zindler, A., Elliott, T., Langmuir, C.H., 1996. Constraints on mantle melting at mid-ocean ridges from global $^{238}U/^{230}Th$ disequilibria data. Nature 384, 231–235.

Bourdon, B., Joron, J.-L., Claude-Ivanaj, C., Allègre, C.J., 1998. U–Th–Pa–Ra systematics for the Grande Comore volcanics: melting processes in an upwelling plume. Earth Planet. Sci. Lett. 164, 119–133.

Bourdon, B., Turner, S.P., Ribe, N.M., 2005. Partial melting and upwelling rates beneath the Azores from a U-series isotope perspective. Earth Planet. Sci. Lett. 239, 42–56.

Bourdon, B., Ribe, N.M., Stracke, A., Saal, A.E., Turner, S.P., 2006. Insights into the dynamics of mantle plumes from uranium-series geochemistry. Nature 444, 713–717.

Boyd, F.R., England, J.L., 1960. Apparatus for phase equilibrium studies at pressures up to 50 kbar and temperatures up to 1750 °C. J. Geophys. Res. 65, 741–748.

Claude-Ivanaj, C., Bourdon, B., Allègre, C.J., 1998. Ra–Th–Sr isotope systematics in Grande Comore Island: a case study of plume–lithosphere interaction. Earth Planet. Sci. Lett. 164, 99–117.

Claude-Ivanaj, C., Joron, J.-L., Allègre, C.J., 2001. ^{238}U–^{230}Th–^{226}Ra fractionation in historical lavas from the Azores: long-lived heterogeneity versus metasomatism fingerprints. Chem. Geol. 176, 295–310.

Cohen, A.S., O'Nions, R.K., 1993. Melting rates beneath Hawaii: evidence from uranium series isotopes in recent lavas. Earth Planet. Sci. Lett. 120, 169–175.

Cohen, A.S., O'Nions, R.K., Kurz, M.D., 1996. Chemical and isotopic variations in Mauna Loa tholeiites. Earth Planet. Sci. Lett. 143, 111–124.

DePaolo, D., 1988. Neodymium isotope geochemistry: An introduction.

Draper, D.S., van Westrenen, W., 2007. Quantifying garnet-melt trace element partitioning using lattice-strain theory: assessment of statistically significant controls and a new predictive model. Contrib. Mineral. Petrol. 154, 731–746.

Elliott, T., 1997. Fractionation of U and Th during mantle melting: a reprise. Chem. Geol. 139, 165–183.

Gaetani, G.A., 2004. The influence of melt structure on trace element partitioning near the peridotite solidus. Contrib. Mineral. Petrol. 147, 511–527.

Gallahan, W.E., Nielsen, R.L., 1992. The partitioning of Sc, Y, and the rare earth elements between high-Ca pyroxene and natural mafic to intermediate lavas at 1 atmosphere. Geochim. Cosmochim. Acta 56, 2387–2404.

Grutzeck, M., Kridelbaugh, S., Weill, D.F., 1974. The distribution of Sr and REE between diopside and silicate liquid. Geophys. Res. Lett. 1, 273–275.

Hauri, E.H., 1996. Major-element variability in the Hawaiian mantle plume. Nature 382, 415–419.

Hauri, E.H., 2002. SIMS analysis of volatiles in silicate glasses, 2: isotopes and abundances in Hawaiian melt inclusions. Chem. Geol. 183, 115–141.

Hauri, E.H., Wagner, T.P., Grove, T.L., 1994. Experimental and natural partitioning of Th, U, Pb, and other trace elements between garnet, clinopyroxene, and basaltic melts. Chem. Geol. 117, 149–166.

Hays, J.F., 1966. Lime–alumina–silica. Carnegie Institution of Washington Yearbook, 65, pp. 234–239.

Hirschmann, M.M., Stolper, E.M., 1996. A possible role for garnet pyroxenite in the origin of the "garnet signature" in MORB. Contrib. Mineral. Petrol. 124, 185–208.

Hirschmann, M.M., Asimow, P.D., Ghiorso, M.S., Stolper, E.M., 1999. Calculation of peridotite partial melting from thermodynamic models of minerals and melts. III. Controls on isobaric melt production and the effect of water on melt production. J. Petrol. 40, 831–851.

Hirschmann, M.M., Kogiso, T., Baker, M.B., Stolper, E.M., 2003. Alkalic magmas generated by partial melting of garnet pyroxenite. Geology 31, 481–484.

Hofmann, A.W., 1988. Chemical differentiation of the Earth: the relationship between mantle, continental crust, and oceanic crust. Earth Planet. Sci. Lett. 90, 297–314.

Johannes, W., Bell, P., Mao, H.K., Boettcher, A.L., Chipman, D.W., Hays, J.F., Newton, R.C., Seifert, F., 1971. An interlaboratory comparison of piston-cylinder pressure calibration using the albite-breakdown reaction. Contrib. Mineral. Petrol. 32, 24–38.

Kogiso, T., Hirschmann, M.M., 2001. Experimental study of clinopyroxenite partial melting and the origin of ultra-calcic melt inclusions. Contrib. Mineral. Petrol. 142, 347–360.

Kogiso, T., Hirschmann, M.M., Frost, D.J., 2003. High-pressure partial melting of garnet pyroxenite: possible mafic lithologies in the source of ocean island basalts. Earth Planet. Sci. Lett. 216, 603–617.

Kogiso, T., Hirschmann, M.M., Pertermann, M., 2004. High-pressure partial melting of mafic lithologies in the mantle. J. Petrol. 45, 2407–2422.

Landwehr, D., Blundy, J.D., Chamorro-Perez, E.M., Hill, E., Wood, B.J., 2001. U-series disequilibria generated by partial melting of spinel lherzolite. Earth Planet. Sci. Lett. 188, 329–348.

Langmuir, C.H., Klein, E.M., Plank, T., 1992. Petrological systematics of mid-ocean ridge basalts: constraints on melt generation beneath ocean ridges. Mantle Flow and Melt Generation at Mid-Ocean Ridges, Geophys. Monograph, 71, pp. 183–280.

Lassiter, J.C., Hauri, E.H., Reiners, P.W., Garcia, M.O., 2000. Generation of Hawaiian post-erosional lavas by melting of a mixed lherzolite/pyroxenite source. Earth Planet. Sci. Lett. 178, 269–284.

La Tourette, T.Z., Burnett, D.S., 1992. Experimental determination of U-partitioning and Th-partitioning between cpx and natural and synthetic basaltic liquid. Earth Planet. Sci. Lett. 110, 227–244.

La Tourette, T.Z., Kennedy, A.K., Wasserburg, G.J., 1993. Thorium–uranium fractionation by garnet: Evidence for a deep source and rapid rise of oceanic basalts. Science 261, 739–742.

Lundstrom, C.C., Shaw, H.F., Ryerson, F.J., Phinney, D.L., Gill, J.B., Williams, Q., 1994. Compositional controls on the partitioning of U, Th, Ba, Pb, Sr, and Zr between cpx and haplobasaltic melts: implications for uranium series disequilibria in basalts. Earth Planet. Sci. Lett. 128, 407–423.

Lundstrom, C.C., Sampson, D.E., Perfit, M.R., Gill, J., Williams, Q., 1999. Insights into mid-ocean ridge basalt petrogenesis: U-series

disequilibria from the Siqueiros Transform, Lamont Seamounts, and East Pacific Rise. J. Geophys. Res. 104, 13,035–13,048.

Lundstrom, C.C., Hoernle, K., Gill, J., 2003. U-series disequilibria in volcanic rocks from the Canary Islands: Plume versus lithospheric melting. Geochim. Cosmochim. Acta 67, 4153–4177.

McDade, P., Blundy, J.D., Wood, B.J., 2003. Trace element partitioning on the Tinaquillo Lherzolite solidus at 1.5 GPa. Phys. Earth Planet. Inter. 139, 129–147.

Nicholls, I.A., Harris, K.L., 1980. Experimental rare earth element partition coefficients for garnet, clinopyroxene, and amphibole coexisting with andesitic and basaltic liquids. Geochim. Cosmochim. Acta 44, 287–308.

Pertermann, M., Hirschmann, M., 2002. Trace-element partitioning between vacancy-rich eclogitic clinopyroxene and silicate melt. Am. Mineral. 87, 1365–1376.

Pertermann, M., Hirschmann, M., 2003. Partial melting experiments on MORB-like pyroxenite between 2 and 3 GPa: Constraints on the presence of pyroxenite in basalt source regions from solidus location and melting rate. J. Geophys. Res. 108.

Pertermann, M., Hirschmann, M.M., Hametner, K., Günther, D., Schmidt, M.W., 2004. Experimental determination of trace element partitioning between garnet and silica-rich liquid during anhydrous partial melting of MORB-like eclogite. Geochem. Geophys. Geosyst. 5.

Pickett, D.A., Murrell, M.T., 1997. Observations of $(^{231}$ Pa$)/(^{235}$U$)$ disequilibrium in volcanic rocks. Earth Planet. Sci. Lett. 148, 259–271.

Pietruszka, A., 1999. The short-term geochemical evolution of Kilauea Volcano, Hawai'i (1790–1998). University of Hawaii.

Ray, G.L., Shimizu, N., Hart, S.R., 1983. An ion microprobe study of partitioning of trace elements between clinopyroxene and liquid in the system diopside–albite–anorthite. Geochim. Cosmochim. Acta 47, 2131–2140.

Salters, V.J.M., Longhi, J., 1999. Trace element partitioning during the initial stages of melting beneath mid-ocean ridges. Earth Planet. Sci. Lett. 166, 15–30.

Salters, V.J.M., Longhi, J.E., Bizimis, M., 2002. Near mantle solidus trace element partitioning at pressures up to 3.4 GPa. Geochem. Geophys. Geosyst. 3.

Shannon, R.D., 1976. Revised effective ionic radii and systematic studies of interatomic distances in halides and chalcogenides. Acta Crystallogr. A32, 751–767.

Sigmarsson, O., Carn, S., Carracedo, J.C., 1998. Systematics of U-series nuclides in primitive lavas from the 1730–36 eruption on Lanzarote, Canary Islands, and implications for the role of garnet pyroxenites during oceanic basalt formations. Earth Planet. Sci. Lett. 162, 137–151.

Sims, K.W.W., Hart, S.R., 2006. Comparison of Th, Sr, Nd and Pb isotopes in oceanic basalts: Implications for mantle heterogeneity and magma genesis. Earth Planet. Sci. Lett. 245, 743–761.

Sims, K.W.W., DePaolo, D.J., Murrell, M.T., Baldridge, W.S., Goldstein, S.J., Clague, D.A., 1995. Mechanisms of magma generation beneath Hawaii and mid-ocean ridges: Uranium/thorium and samarium/neodymium isotopic evidence. Science 267, 508–512.

Sims, K.W.W., DePaolo, D.J., Murrell, M.T., Baldridge, W.S., Goldstein, S., Clague, D., Jull, M., 1999. Porosity of the melting zone and variations in the solid mantle upwelling rate beneath Hawaii: Inferences from ^{238}U–^{230}Th–^{226}Ra and ^{235}U–^{231}Pa disequilibria. Geochim. Cosmochim. Acta 63, 4119–4138.

Sims, K.W.W., Goldstein, S.J., Blichert-Toft, J., Perfit, M.R., Kelemen, P., Fornari, D.J., Michael, P., Murrell, M.T., Hart, S.R., DePaolo, D.J.,

Layne, G., Ball, L., Jull, M., Bender, J., 2002. Chemical and isotopic constraints on the generation and transport of magma beneath the East Pacific Rise. Geochim. Cosmochim. Acta 66, 3481–3504.

Sims, K.W.W., Hart, S.R., Reagan, M.K., Blusztajn, J., Staudigel, H., Sohn, R.A., Layne, G.D., Ball, L.A., Andrews, J., in press. ^{238}U–^{230}Th–^{226}Ra–^{210}Pb–^{210}Po, ^{232}Th–^{228}Ra and ^{235}U–^{231}Pa constraints on the ages and petrogenesis of Vailulu'u and Malumalu Lavas, Samoa. Geochem. Geophys. Geosyst.

Sobolev, A.V., 2000. Recycled oceanic crust observed in 'ghost plagioclase' within the source of Mauna Loa lavas. Nature 404, 986–990.

Spiegelman, M., Elliott, T., 1993. Consequences of melt transport for U-series disequilibrium in young lavas. Earth Planet. Sci. Lett. 118, 1–20.

Stracke, A., Salters, V.J.M., Sims, K.W.W., 1999. Assessing the presence of garnet-pyroxenite in the mantle sources of basalts through combined hafnium–neodymium–thorium isotope systematics. Geochem. Geophys. Geosyst. 1.

Turner, S.P., Hawkesworth, C., Rogers, N., King, P., 1997. U–Th isotope disequilibria and ocean island basalt generation in the Azores. Chem. Geol. 139.

Ulmer, P., Luth, R.W., 1991. The graphite-COH fluid equilibrium in P, T, fO2 space. Contrib. Mineral. Petrol. 106, 265–272.

van Westrenen, W., Blundy, J.D., Wood, B.J., 1999. Crystal-chemical controls on trace element partitioning between garnet and anhydrous silicate melt. Am. Mineral. 84, 838–847.

van Westrenen, W., Blundy, J.D., Wood, B.J., 2000. Effect of Fe^{2+} on garnet-melt trace element partitioning: Experiments in FCMAS and quantification of crystal-chemical controls in natural systems. Lithos 53, 189–201.

van Westrenen, W., Wood, B.J., Blundy, J.D., 2001. A predictive thermodynamic model of garnet-melt trace element partitioning. Contrib. Mineral. Petrol. 142, 219–234.

Widom, W., Carlson, R.W., Gill, J.B., Schmincke, H.U., 1997. Th–Sr–Nd–Pb isotope and trace element evidence for the origin of the Sao Miguel enriched mantle source. Chem. Geol. 140, 49–68.

Wood, B.J., Blundy, J.D., 1997. A predictive model for rare earth element partitioning between clinopyroxene and anhydrous silicate melt. Contrib. Mineral. Petrol. 129, 166–181.

Wood, B.J., Blundy, J.D., Robinson, J.A.C., 1999. The role of clinopyroxene in generating U-series disequilibrium during mantle melting. Geochim. Cosmochim. Acta 63, 1613–1620.

Workman, R.K., Hart, S.R., 2005. Major and trace element composition of the depleted MORB mantle (DMM). Earth Planet. Sci. Lett. 231, 53–72.

Workman, R.K., Hart, S.R., Jackson, M., Regelous, M., Farley, K.A., Blusztajn, J., Kurz, M., Staudigel, H., 2004. Recycled metasomatized lithosphere as the origin of the Enriched Mantle II (EM2) end-member: evidence from the Samoan Volcanic Chain. Geochem. Geophys. Geosyst. 5.

Workman, R.K., Hauri, E., Hart, S.R., Wang, J., Blusztajn, J., 2006. Volatile and trace elements in basaltic glasses from Samoa: implications for water distribution in the mantle. Earth Planet. Sci. Lett. 241, 932–951.

Zindler, A., Hart, S., 1986. Chemical geodynamics. Annual reviews in earth and planetary. Science 11, 493–571.